nature communications

Article

https://doi.org/10.1038/s41467-024-50923-8

Holographic direct sound printing

Received: 30 November 2023

Accepted: 24 July 2024

Published online: 06 August 2024

Check for updates

Mahdi Derayatifar[1], Mohsen Habibi[2], Rama Bhat[1] & Muthukumaran Packirisamy[1]

Direct sound printing (DSP), an alternative additive manufacturing process driven by sonochemical polymerization, has traditionally been confined to a single acoustic focal region, resulting in a voxel-by-voxel printing approach. To overcome this limitation, we introduce holographic direct sound printing (HDSP), where acoustic holograms, storing cross-sectional images of the desired parts, pattern acoustic waves to induce regional cavitation bubbles and on-demand regional polymerization. HDSP outperforms DSP in terms of printing speed by one order of magnitude and yields layerless printed structures. In our HDSP implementation, the hologram remains stationary while the printing platform moves along a three-dimensional path using a robotic arm. We present sono-chemiluminescence and high-speed imaging experiments to thoroughly investigate HDSP and demonstrate its versatility in applications such as remote ex-vivo in-body printing and complex robot trajectory planning. We showcase multi-object and multi-material printing and provide a comprehensive process characterization, including the effects of hologram design and manufacturing on the HDSP process, polymerization progression tracking, porosity tuning, and robotic trajectory computation. Our HDSP method establishes the integration of acoustic holography in DSP and related applications.

Direct sound printing (DSP)[1] is a class of additive manufacturing (AM) processes introduced recently by our research group in which chemically active acoustic cavitation bubbles derive polymerization in focal regions of an acoustic field in a printing resin medium. DSP differentiates itself from other AM methods mainly on the energy source and the chemical activation. AM processes utilize either light[2–4] or heat[5–7] for deriving chemical reactions or physical transformation. However, DSP employs sonochemistry, which utilizes the dynamic behavior of cavitation bubbles within an acoustic field. During the sonochemical process, these cavitation bubbles undergo rapid oscillations, expanding during periods of low pressure and collapsing violently under high pressure. The collapse of these bubbles generates localized hot spots where temperatures and pressures can reach extreme levels[8–10] sufficient momentarily to break and form chemical bonds or also create ones. This intense environment within the bubbles enables various chemical reactions, crucial for the DSP process, allowing for precise manipulation of the material's polymerization at microscopic scales. Cavitation, once predominantly viewed as a destructive force[11], has recently become the focus of exploration for beneficial and innovative outcomes. This includes applications in medical and biomedical[12], environmental management[13] and industrial processing[14]. DSP also leverages the cavitation phenomena for creation. DSP is a unique AM method enabling the direct printing of materials, such as heat-curing thermosets, which are difficult to process with light or heat. Moreover, DSP introduced a new paradigm in AM called remote distance printing (RDP)[1] in which the possibility of printing beyond optically opaque and non-transparent obstacles is presented.

Our pioneering works on DSP and RDP[1,15–17] have garnered significant interest, igniting new research into ultrasound-driven 3D printing. We introduced the paradigm of printing through physical barriers, such as directly inside the human body[1]. The concept of

[1]Optical Bio Microsystems Laboratory, Micro-Nano-Bio Integration Center, Department of Mechanical, Industrial and Aerospace Engineering, Concordia University, Montreal, QC, Canada. [2]Department of Mechanical and Aerospace Engineering, University of California at Davis, Davis, CA, USA.
e-mail: m.packirisamy@concordia.ca

non-invasive deep printing inside the body was initially demonstrated ex vivo[1]. The chemical reactivity induced by ultrasound sources arises from a mix of thermochemistry, caused by heat generation through acoustic attenuation, and sonochemistry, resulting from acoustic cavitation bubbles. Notably, the temperature rises at the macroscopic scale of the focal region due to acoustic attenuation were insufficient to facilitate on-demand curing in materials like silicone elastomers or epoxies through thermochemistry alone; hence, sonochemical reactions within the cavitation bubbles have been proposed to enable on-demand curing for such materials. Later, hydrogels have been successfully printed using DSP to reaffirm the concept of in-body printing[18,19]. Recently, an ultrasonic horn with a concave front surface has been used as the primary ultrasound source to create an acoustic focal region and print filaments of thermoset materials[20]. Additionally, a cost-effective sound-based 3D printer has been developed, capable of solidifying silicone elastomer and egg white[21]. In all of the above-mentioned works on DSP, single-focal ultrasound sources have been utilized.

Similar to stereolithography (SLA) in which a single laser spot is the only chemically active region, we had presented the same single active region concept in our initial work[1] to present DSP for the first time. This was mainly due to implementation simplicity. Therefore, DSP suffers similar to SLA (or single nozzle extrusion-based deposition modeling[5,22] or direct ink writing[3,23]) from the fact that only one voxel at a time can be created. To remedy this in the concept of SLA, the utilization of digital light processing (DLP)[24,25] was introduced in which a cross-section image is flashed on the entire printing platform to cure the whole layer at once. Later on, the concept of volumetric printing[26,27] emerged in which instead of cross-section the entire volume of the part is created almost instantly. In addition, sequential illumination via projected tomography[28–31] made a substantial advances in the volumetric additive manufacturing field as well.

DSP lacks similar concepts to bring the current voxel-by-voxel DSP to the next level by creating a cross-section or the whole part volume at once. In the present paper, we introduce a DSP method in which the polymerization occurs at a cross-section at once instead of point-by-point. We accomplished this by utilizing acoustic holography to create patterns of acoustic pressure at specific image planes where the part's cross sections are supposed to be created. The derived polymerization resulting from induced cavitation bubbles is distributed over the whole pressure pattern and in the desired regions, in contrast to a focused point in DSP[1].

In order to pattern pressure waves, one approach is to use phased array transducers (PATs) since each element is driven independently and they have dynamic wave-controlling capability. However, they greatly suffer from generating a very low-resolution acoustic field since their element counts are limited and elements are larger in size compared to the wavelengths in MHz frequency. In addition, they have a drawback of requiring complicated electrical equipment and synchronization[32–34]. This made us to implement the concept of the present paper by acoustic holograms. Acoustic holograms or metamaterials are alternatives to PATs with a higher degree of freedom in manipulating the sound field[35–39]. They possess high information content that can create intricate arbitrary sound fields while offering an inexpensive and simple setup. A plethora of applications has been employed via acoustic holography using transmission acoustic holograms including cell and particle patterning[33,40,41], medical imaging[42], hyperthermia treatment[43], neurostimulation and transcranial therapy[44,45] and particle assembly[46,47].

Here in this paper, we present a holography-based DSP process, or in short HDSP, in which the information of the cross sections of the part to be printed are stored in an acoustic hologram. During the sonication of the printing material, the active cavitation bubbles are generated at the target images while the printing material polymerizes instantly. Figure 1a shows the concept of HDPS schematically where the acoustic holography source, in this case a passive monolithic 3D printed hologram, is attached to a single-element flat transducer. Employing the acoustic holography as an advanced acoustic manipulation tool has shown reduced printing time while being energy efficient compared with the point-based DSP.

Results

We stored the information of the printed part in the hologram developed using the iterative angular spectrum (IAS) method[35] and 3D printed the hologram using SLA. The build chamber is positioned in front of the hologram and filled with the printing material (see section "Methods"). The transducer, hologram and the bottom face of the build chamber are submerged in the transmitting water medium. The hologram coordinate system is stationary and attached to the surface of the hologram. The ultrasound wave patterned by the hologram passes through the thin build chamber bottom face and a portion of the build material until it reaches to a printing platform. The front face of the printing platform is located at the image plane location. The platform is moved in space by a motion manipulator, a robot, along a three-dimensional path which is calculated for the desired part. The platform is attached to the end effector of a robot. The end-effector coordinate system moves with respect to the hologram coordinate system. Since the platform is located at the image plane at the beginning of the process, the cavitation bubbles are generated at the desired image creating ultra-active micro reactors[1] region and polymerizing the printing material on the platform or previously solidified region of the part as shown in Fig. 1b. The platform is placed at the target image plane where the acoustic pressure more than the threshold for printing is reached. Moreover, due to the low viscosity medium, the platform is needed to adhere to the already solidified part. By moving the platform along z-axis by feed, f, the part is generated as an extruded object along z-axis as portion I in Fig. 1a. By rotating the platform about z-axis at an angular velocity, ω, and extruding by feed f, an extruded and twisted object can be created as portion II in Fig. 1a. Figure 1c shows printed letters "D", "S" and "P" and their corresponding theoretical pressure patterns created by their hologram at the image plane. Figure 1d shows a more complicated maple leaf printed object and its theoretical pressure pattern at the image plane. The platform is stationary in Fig. 1c, d. Figure 1e is a 15 mm long printed wall where its hologram creates a pressure pattern of a line at the image plane on the platform and the platform is moved continuously to create the extruded wall along $+z$-direction (Supplementary Movies 1 and 2). Figure 1f shows the incorporation of the rotation to the platform while translation in z-direction using the same holograms that project the line image on the platform (Supplementary Movie 3). The printed helix in Fig. 1f represents successful unsupported features printing in HDSP by tuning the printing platform motion velocity and the patterned intensity. Beyond translational and rotatory movements of the platform as in Fig. 1e, f, HDSP enables the printing geometries along a free-from path. However, the robot's trajectory for such parts needs to be calculated based on our developed algorithms presented in the "Methods" section. Figure 1g shows a U-shaped part printed with the same hologram as in Fig. 1e, f with a line image without any support. The printing platform was attached to the end effector of a robotic arm (Supplementary Movie 4). More examples of printing parts with unsupported features will be discussed.

The printed objects in HDSP are layerless as can be seen in Fig. 1c–g, with a relatively shorter printing time, in comparison with point-DSP. Quantitatively, a wall such as in Fig. 1e with the 15 mm width and 20 mm height with HDSP takes only ~30–90 s, while the point-based DSP[1], that uses a single chemically active region, takes ~4–13 min. We have further conducted detailed analyses of the printing processes for HDSP and DSP, focusing on power consumption and total energy deposition. Both simulation and experimental data were analyzed for printing a wall with identical dimensions using both methods. Our

https://doi.org/10.1038/s41467-024-50923-8

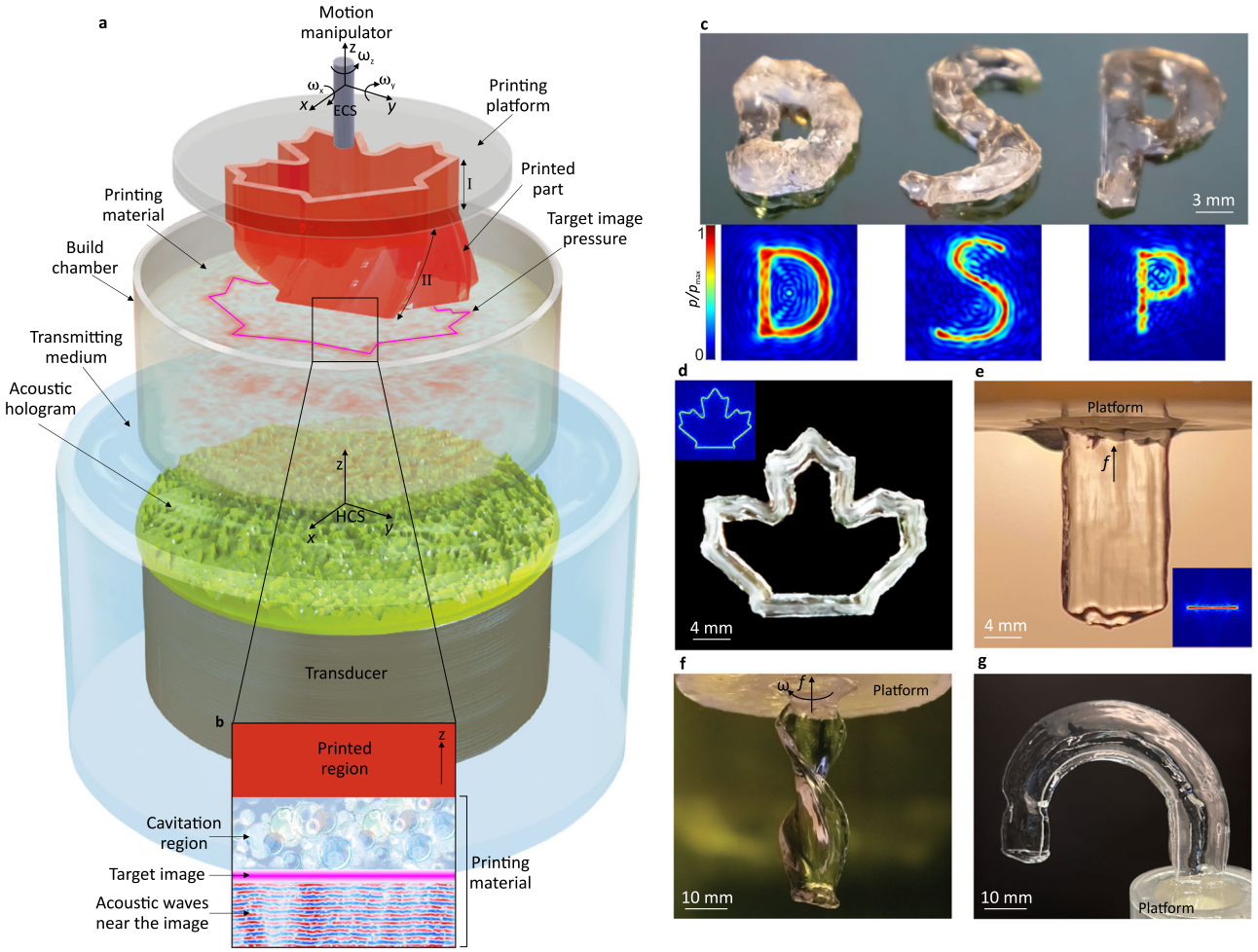

Fig. 1 | HDSP concept and printed objects. a Schematic of HDSP process with the printed part on a platform mounted on a robotic end effector, showing the end-effector coordinate system (ECS) and translational (xyz) and rotational (ω_x, ω_y, ω_z) degrees of freedom. **b** Detailed view of the printing region, cavitation bubbles are created near the target pressure image. **c** Printed "DSP" letters, printing parameters: $P = 20$ W, $f_0 = 2.28$ MHz, $DC = 35\%$, with their corresponding simulated pressure patterns, p, normalized to the maximum pressure, p_{max}. **d** Printed maple leaf, printing parameters: $P = 25$ W, OD = 50 mm, $f_0 = 2.28$ MHz, DC = 30%. **e** Fully transparent printed wall axially extruded/printed by feed, f, along +z-axis, printing parameters: $P = 6$ W, OD = 25 mm, $f_0 = 2.24$ MHz, DC = 20%. **f** Transparent printed helix by translational and rotational motions of the platform in multi-axis HDSP. **g** Self-supported U-shape object printed via computed robot trajectory using the same printing condition as (**e**). OD, P, f_0 and DC are transducer aperture size, acoustic power, acoustic center frequency and duty cycle, respectively.

findings reveal that while DSP requires less power per unit of time, it consumes more total energy due to its longer operational time compared to HDSP. Furthermore, although DSP exhibits a higher energy density, suggesting intense energy use per unit volume, HDSP compensates for this with substantially faster printing times, making it highly advantageous for applications that require quick production without significantly compromising on energy efficiency. These insights are further elaborated in Supplementary Table 2, which details the comparative analyses. The volume deposition rate in HDSP is also quantified in Supplementary Table 1.

Similar to DSP, printing parameters in HDSP also affect the microstructure, resolution and printing time. Printing parameters include output acoustic power, P, center frequency, f_0, duty cycle, DC% (the active fraction of the driving pulse period), printing material mixing ratio and the platform velocity[1]. Since the acoustic power is being distributed in the image pixels of the target plane, if the image has more complexity, the acoustic power should be increased as well to supply enough power at the image to induce cavitation and derive polymerization. We adjusted the acoustic power ranging from 5 to 25 W depending on the part complexity to have enough pressure (~2 MPa, this pressure threshold is critical for initiating the sonochemical reactions required for the polymerization process in PDMS) in the image plane pixels required for printing. We have found that increasing the emitted power or acoustic pressure beyond this threshold disturbs the pattern uniformity. This disturbance occurs because the excessive acoustic force generates streaming within the resin, negatively impacting the print quality. In addition, due to the unique pressure amplification of each acoustic pattern, the input acoustic power is compensated and tuned so that enough acoustic energy is transferred to the desired voxels simultaneously to ensure the activation of sonochemical reactions. The line pattern that we used to print a wall type in Fig. 1e, required only 6 W acoustic power and 20% DC with a relatively high rate of solidification, while more complex geometric shape such as the maple leaf in Fig. 1d, requires 25 W acoustic power to derive the solidification process at desired locations. DC of the ultrasound signal affects the microstructure. Lowering DC helps with more transparent and less porous structures. DC 20% results in fully transparent parts while DC 100% results in fully non-transparent and porous structures. Another affecting factor in HDSP on the resolution is the spatial dimension of the transmission phase plate which affects the space-bandwidth product of the transmission phase plate[35]. The larger transducer's transmitting surface area with the same center frequency can incorporate a denser phase pattern resulting in a more complex acoustic field with finer resolution which is

suitable for complex patterns. Here, the printed wall in Fig. 1e is created from extruding a line with a 25 mm diameter transducer, while for complex geometries such as the maple leaf in Fig. 1d, a transducer with a 50 mm diameter is used.

Further enhancing resolution can theoretically be addressed by utilizing higher frequencies. For instance, a frequency of 3.5 MHz could significantly improve pattern uniformity and the sound-to-noise ratio (SNR), due to increased spatial resolution allowing the hologram to reconstruct with richer details. However, a notable trade-off at higher frequencies is the reduced acoustic penetration depth, a consequence of increased material attenuation. This limitation restricts the effective range of sound waves within the material, posing challenges for deeper or thicker structures.

HDSP concept inception through sonochemiluminescence (SCL) experiments

The idea of HDPS originates from our SCL experiments where we pattern the acoustic waves at the image plane in an aqueous solution of luminol (3-aminophthalhydrazide). We observed that at the image plane, a blue light pattern is emitted due to sonochemical reactions of hydroxyl radical and hydrogen peroxide with luminol[48–50]. This observation proved that localized chemical reactions at the desired target plane could be created using the acoustic holograms through cavitation bubbles generation at the image pixels. Figure 2 shows the experimental setup schematically where a digital single-lens reflex (DSLR) captures the image plane illumination during 30 s exposure time in a dark room. Figure 2b–e shows the illuminated patterns and their corresponding theoretical acoustic pressure patterns produced by the holograms in the luminol solution. As it can be seen, there is a good agreement between the desired pressure pattern and the illuminated regions. Figure 2b, c is created by a transducer 25 mm diameter, while a transducer with a 50 mm diameter is used for Fig. 2d, e due to higher image complexity.

High-speed imaging of HDSP

We captured the HDSP process using shadowgraph and Schlieren photography concepts[1] via high-speed imaging as shown schematically in Fig. 3a. For this set of experiments, the holograms are designed for

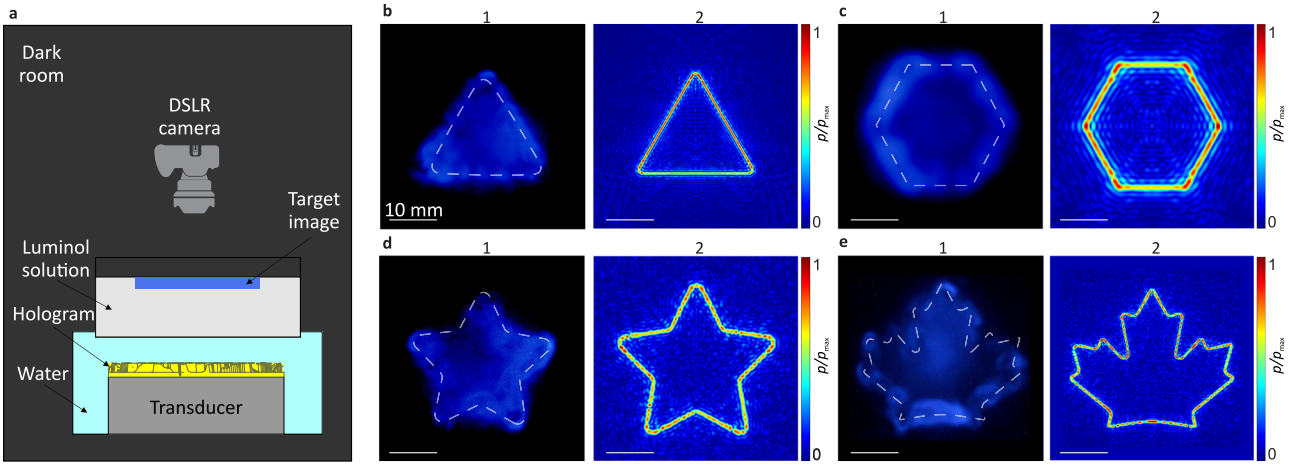

Fig. 2 | SCL experiments to demonstrate the patternability of chemical reactions using holograms. a SCL setup including a DSLR camera capturing top view of the luminol solution surface. **b1**–**e1** Captured luminol illumination patterns. **b2**–**e2** Corresponding theoretical acoustic pressure map at the target plane. Acoustic parameters used in (**b**) are OD = 25 mm, f_0 = 2.24 MHz, DC = 100%, P = 15 W, in (**c**) are OD = 35 mm, f_0 = 1.86 MHz, DC = 100%, P = 20 W, and in (**d**, **e**) are OD = 50 mm, f_0 = 2.28 MHz, DC = 100%, P = 25 W.

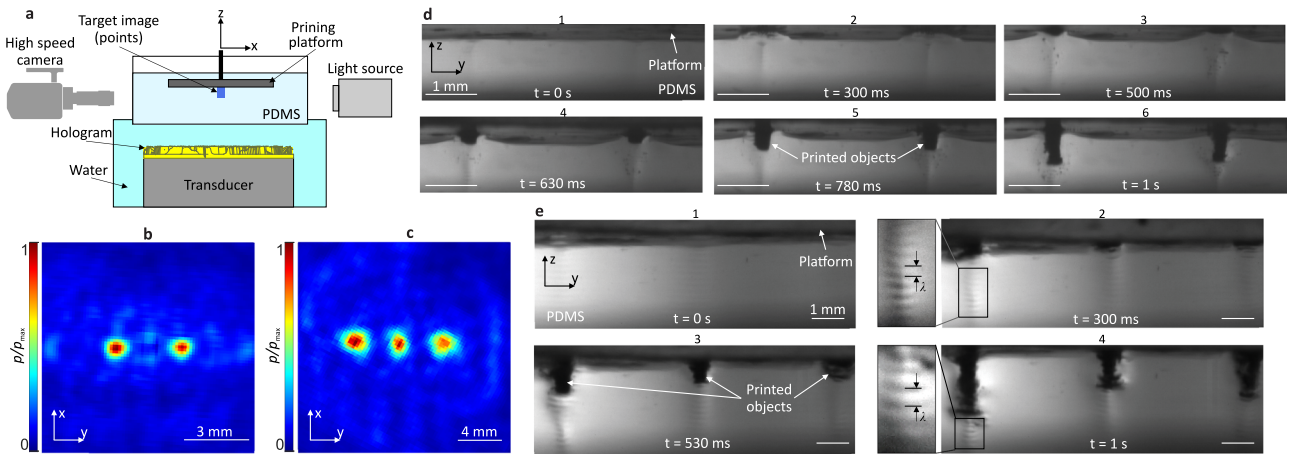

Fig. 3 | Close observation of the HDSP printing process employing high-speed imaging. a Side view of the observation setup including a high-speed camera to capture the HDSP printing process. **b**, **c** Normalized measured pressure maps of designed two- and three-spot pressure images, respectively. The gap between each two spots is 3 mm in (**b**) and 4 mm in (**c**). **d** Footage of high-speed imaging for two spots being printed with HDSP process during 1 s insonication. **e** Footage of high-speed imaging for three-spot printing during 1 s insonication. In all cases the platform (image plane) is designed to be 20 mm away from the transducer, printing parameters: OD = 25 mm, P = 5 W, f_0 = 2.24 MHz, DC = 50%.

two- and three-point images at the image plane and Fig. 3b, c shows the measured pressure patterns for these holograms, respectively. While the platform stays still, pillar objects are printed at the locations of the points at the image plane. Figure 3d, e shows the footage during 1 s sonication (Supplementary Movies 5 and 6). Detailed views of Fig. 3e2, e4 show the high- and low-pressure zones with a wavelength of $\lambda = \lambda_0/2$ (where λ_0~370 µm is sound wavelength in our printing material, polydimethylsiloxane (PDMS)) in the chemically active region which was previously observed in the case of a single point of focused ultrasound as well and known as ultra-active micro reactors[1].

Special applications

Multi-object/location printing. One of the distinct features of acoustic holography is the capability to store the information content of multiple images in a single hologram. These images can be located in different locations or levels in space. Therefore, multiple objects can be created simultaneously at different locations in the printing space. Figure 4a shows this concept where the images of three points at three target *z*-levels are stored in a single hologram and a complex pressure pattern is created in the printing space. If a multi-level platform was located at the target levels and being moved along +*z*-axis, three extruded pillars could be created at the same time on the three levels of the platform. Figure 4b shows the multi-level printing platform for this experiment in which three pillars are printed on their levels. The simulated reconstruction field is shown in Figure 4a.

The HDSP's ability to encode information content for multiple objects thanks to the precise control on acoustic holography, allows for innovative applications such as complex tissue structures, localized drug and cell delivery systems, and advanced tissue engineering. For instance, it enables the printing of multi-layered tissue structures like skin grafts with distinct layers (dermis and epidermis), each tailored with different cells and growth factors for enhanced healing. Additionally, HDSP can be used to create drug-loaded structures within a gel matrix at targeted locations, crucial for combination therapies where different therapeutic agents are released at specific sites. Furthermore, the technology supports the creation of tissue engineering scaffolds with gradient distributions of growth factors or cells, promoting organ repair and regeneration. These capabilities demonstrate HDSP's potential to address complex biomedical challenges, though further development and interdisciplinary collaboration are essential for optimizing material properties and printing parameters for clinical applications.

The effectiveness of HDSP in generating multiple objects with distinguishable and high-fidelity results depends on maintaining specific separation distances. This separation correlates directly with the spatial bandwidth of the acoustic hologram and the diameter of the transducer. Smaller transducer diameters and limited hologram bandwidth allow for the creation of simpler geometries, such as various lines and points. Conversely, utilizing larger acoustic field areas enables the incorporation of more complex shapes. Furthermore, the reconstruction of more complex images using HDSP requires increased separation distances between objects to ensure high-fidelity outcomes. The details of the reconstructions with various transducer diameters are depicted in Supplementary Fig. 6.

Remote distance printing. We used the HDSP method for the concept of RDP[1] in which an object is printed behind multiple optically non-transparent mediums and physical obstacles. This a unique application of DSP and HDSP owing to the inherent characteristics of the sound waves that can pass through opaque mediums as long as the acoustic coupling is maintained. We added green dye to the printing material to make it opaque and then printed a wall as seen in Fig. 4c where the ultrasound travels through the solid bottom face of the build chamber and passed 10 mm optically opaque printing material and reaches to the moving printing platform along +*z*-axis.

A unique application of RDP is its potential to facilitate printing inside the body[1]. We investigated this concept with an ex-vivo experiment where printing occurred behind a porcine tissue. Figure 4d illustrates this concept using the HDSP method to print non-invasively beyond the porcine tissue. The tissue contains skin, fat and muscle layers shown in the detailed view of Fig. 4d. Figure 4e shows the remotely printed helix while the patterned pressure waves are passing through the porcine tissue. Furthermore, more complex pattern than a line can be used in HDSP for the purpose of RDP to print through optically opaque obstacles and materials. To demonstrate this, we loaded green dye to the printing material to make it opaque and then printed a maple leaf object (Fig. 4f, Supplementary Movie 7).

Overprinting. We explored the concept of overprinting in HDSP by printing a structure with a hologram and overprinting on that structure by switching the hologram to another. The circular part of Fig. 4g1 is created by a stationary platform and a hologram with a stored image of a circle. Then the hologram is changed to the one with two parallel lines as a stored image and the platform is moved vertically to create two parallel extruded walls on top of the already printed circle as shown in Fig. 4g2.

Multi-material printing. Multi-material printing concept is feasible with HDSP by changing the printing material during the print process as shown in Supplementary Fig. 2a, b where we printed a wall with different colors. In order to achieve multi-material printing, the build chamber is replaced with another build chamber filled with the new printing material. Changing the build chamber could create referencing errors that are clearly seen on the multi-material printed wall in Supplementary Fig. 2b.

Robot's trajectory in HDSP. The printing platform is attached to a robot's end effector in HDSP (Fig. 5a, Supplementary Movies 8–10). This enables us to move the printing platform along a complex path, which results in multi-axis printing with overhanging features. An in-plane (*xz*) motion of the robot's end-effector results in the printed object in Fig. 5b (Supplementary Movie 11). Platform rotation about *z*-axis, coupled with upward movement in +*z*-direction, enables the creation of a helical object, as was shown in Fig. 5c. For more complex extrusion path, the robot trajectory is computed (section "Methods") to maintain the constant printing speed and orientation at the image plane. A flexible, self-supporting U-shape part (Fig. 5d, Supplementary Movie 4) is printed using the calculated trajectory shown in Fig. 5e–h schematically. The path generation and kinematics for the robotic arm are discussed in the "Methods" section and shown in Supplementary Fig. 7.

HDSP process characterization

The accuracy of printing objects using HDSP depends heavily on the accuracy of projected target images, which is controlled by the accuracy of manufactured holograms. The manufacturing process of the holograms creates error on the phase plates and consequently causes distortion and unwanted regions on the desired image at the target planes. The holograms in this paper are manufactured using an SLA 3D printer with a nominal resolution of 125 µm (~$\lambda_w/5$, where λ_w is the sound wavelength in water at 2.2 MHz). We manufactured a hologram with a maple leaf as the stored image and then the surface of the printed hologram is 3D scanned with a confocal microscopy method with an accuracy of $\lambda_w/8$ and compared it with the theoretical hologram. The normal surface deviation between the manufactured and theoretical hologram is shown in Fig. 6a. Less than 30% of the scanned surface of the manufactured hologram has more than 150 µm deviations with respect to the theoretical hologram. Such deviation could cause image distortion and inaccuracy of the printed part. We simulated the pressure pattern at the target plane for both manufactured and theoretical holograms using linear acoustics (section "Methods")

https://doi.org/10.1038/s41467-024-50923-8

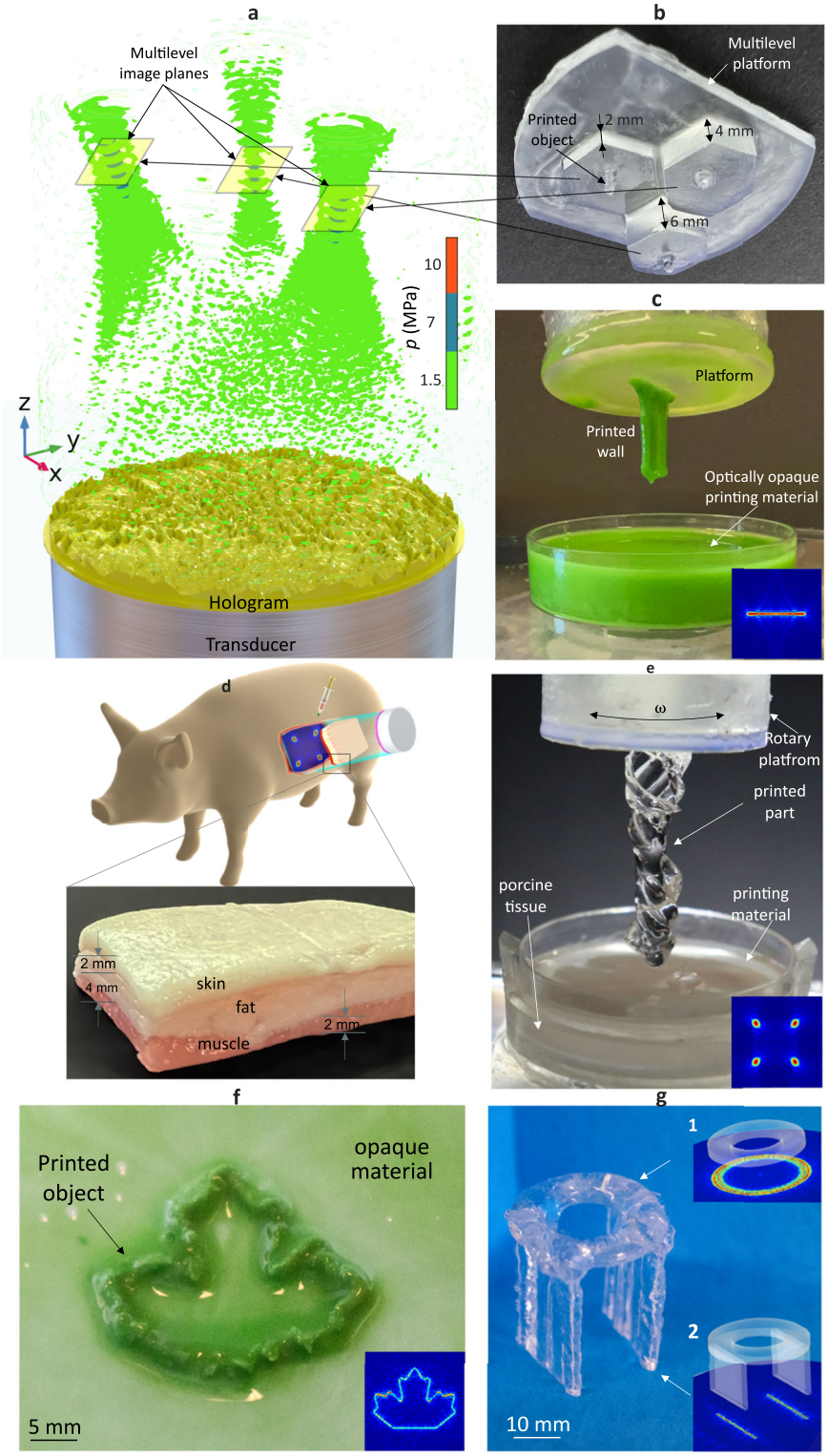

Fig. 4 | Especial Applications of HDSP. a Simulated pressure field of multi-target image planes creating multiple spots in one shot. **b** Printed various spots in one shot on multi-level platform using a single acoustic hologram. **c** Printing in non-transparent material enabling remote distance printing (RDP) applications. **d** Schematic of the idea of on-invasive printing within a living organism through the RDP concept. The zoomed view details the porcine tissue layers employed in the RDP experiment. **e** Printed twisted helix over the barrier including porcine tissue shown in (**d**). Printing parameters: OD = 25 mm, $P = 8$ W, $f_0 = 2.24$ MHz, DC = 50%. **f** Printed maple leaf in non-transparent material as another example of RDP. Printing parameters: OD = 50 mm, $P = 25$ W, $f_0 = 2.85$ MHz, DC = 50%. **g** An example of overprinting possibility in HDSP, where two walls are printed over the printed hollow circular shell. The fabrication steps are shown in **g**1 and 2.

as shown in Fig. 6b-left and right, respectively. The inaccuracies in the manufactured hologram cause an uneven pressure pattern and unwanted pressure lobes (Fig. 6b-right) in comparison with the theoretical hologram's pressure pattern (Fig. 6b-left). Uneven pattern with unwanted high-pressure regions creates printing inaccuracies in the HDPS process. Therefore, the proper manufacturing process selection of holograms has a prime importance in HDSP to achieve accurate printed parts.

https://doi.org/10.1038/s41467-024-50923-8

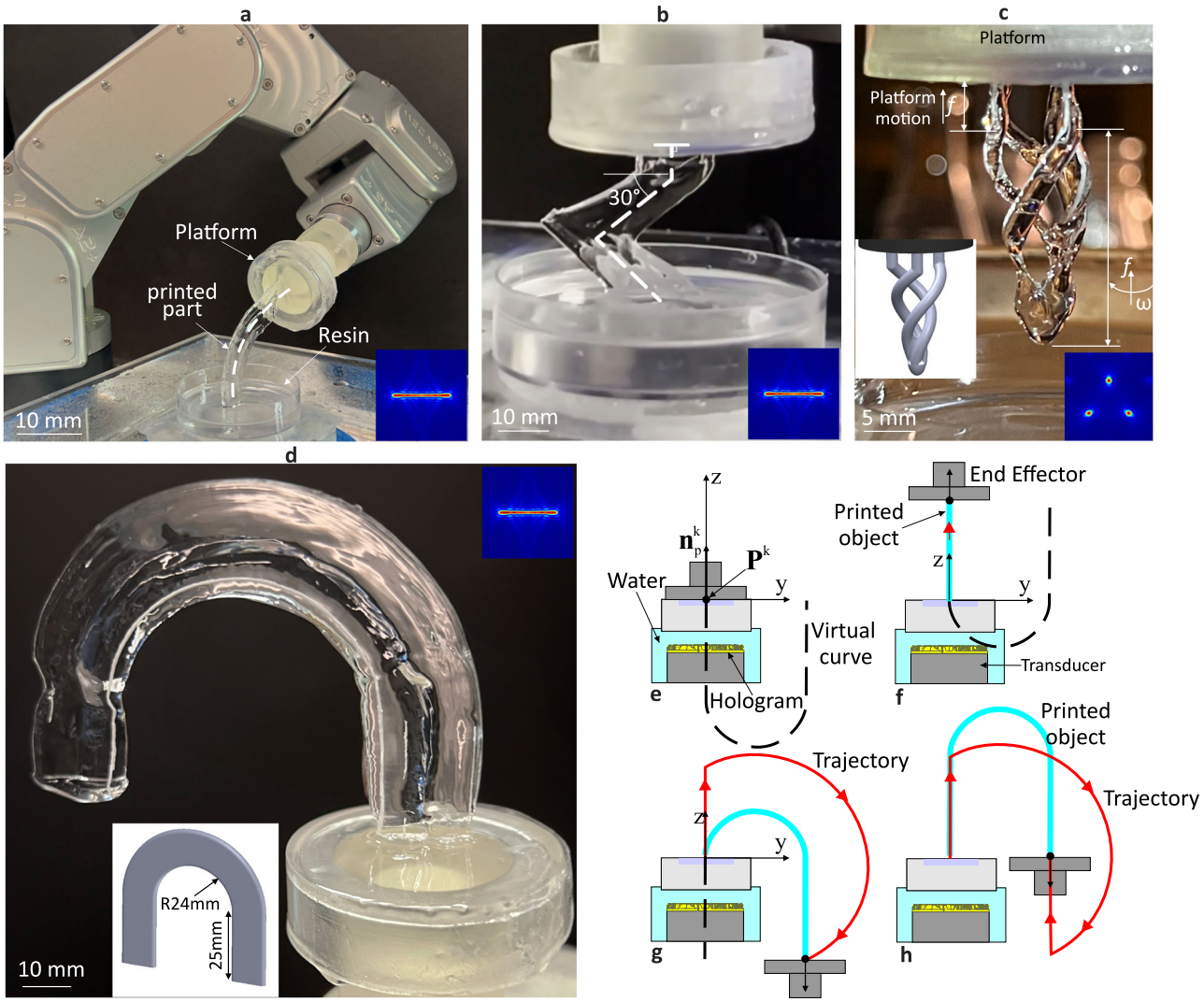

Fig. 5 | Robot-assisted HDSP. a Experimental setup comprising a printing platform which is mounted to a robotic arm's end-effector and an arc being printed with the corresponding pressure pattern. **b** An object with the in-plane extrusion path. **c** Helical object created by rotation about the *z-axis* with variable feed while being extruded in +*z*-direction with constant feed. The pressure pattern used is shown in the inset. The inset shows the 3D model of the intended part. **d** Unsupported *U*-shape part formed with computed robot trajectory. **e**–**h** Schematic of the printing process of (**d**) and computed trajectory.

In exploring the resolution capabilities of HDSP, it is crucial to understand the physical limitations imposed by the principles of acoustic holography. The resolution of HDSP is primarily governed by the wave interference patterns and the wavelength, λ, of the acoustic waves utilized. Theoretically, the acoustic hologram is capable of achieving a diffraction-limited resolution of ~$\lambda/2$ in areas of higher pressure. However, in practical implementations, the actual reconstructed image often exhibits a thickness around λ. This discrepancy arises due to diffraction effects and interference that soften sharp edges or cause blending in the reconstructed image, as can be seen in the inset of Fig. 6b.

Moreover, beyond the acoustic parameters, the DC (which mainly corresponds to the transparency and porosity) in HDSP significantly influences the final print resolution. Experimental observations indicate that higher DC settings enhance resolution by increasing the precision in energy delivery to the target regions. Conversely, lowering the DC leads to reduced resolution.

In addition, the accuracy of the printed parts can be improved by selecting a proper ultrasound center frequency, f_0, and transducer active diameter, OD. Figure 6c illustrates an example of a mandala pattern (Fig. 6c-middle) created by two different frequency and traducer size sets. A low-resolution image pattern (Fig. 6c-left) is created by OD = 25 mm and f_0 = 1.5 MHz while a high-resolution image pattern (Fig. 6c-right) is produced by OD = 64 mm and f_0 = 4.5 MHz. Figure 6d, e shows produced target image quality analyses' results based on Correlation and normalized mean squared error (NMSE) criteria (section "Methods") for feasible ranges of OD and f_0. The case of Fig. 6c-left possesses the lowest value of Correlation and highest value of NMSE while the case of Fig. 6c-right possesses the highest value of Correlation and lowest value of NMSE. Therefore, theoretically, increasing of OD and f_0 improves the image quality and consequently the accuracy of the printed parts. However, there is a limitation on how much f_0 could be increased. Increasing f_0 results in increasing the acoustic attenuation of the printing medium and loss of acoustic energy reaching to the platform. This limitation restricts the effective range of sound waves within the material, posing challenges for deeper or thicker structures. Therefore, there is an optimum value for f_0 based on the printing setup and the printing material used. Other evaluating parameters such as peak sound-to-noise ratio (PSNR) and Structural Similarity Index Measure (SSIM) shown in Supplementary Fig. 5a, b confirm that fine-tuning field frequency and spatial field.

https://doi.org/10.1038/s41467-024-50923-8

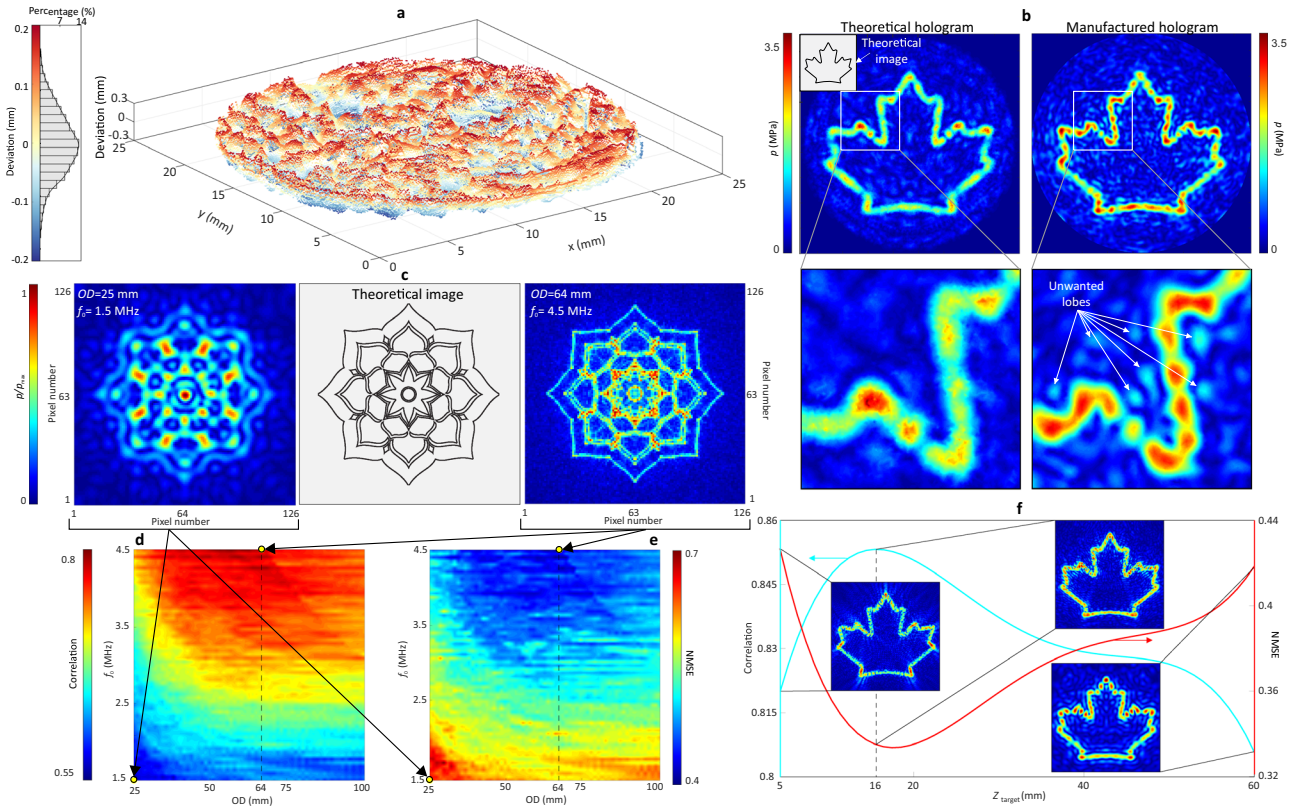

Fig. 6 | Hologram-related process characterization of HDPS. a Surface deviation and deviation distribution between manufactured and theoretical holograms. **b** Pressure patterns obtained via finite element analysis for the theoretical hologram (**b**-left) and scanned manufactured hologram (**b**-right). **c** Image and printing resolution investigation by changing OD and f_0, a theoretical mandala image (**c**-center) is constructed in low resolution (**c**-left) by OD = 25 mm, f_0 = 1.5 MHz and high resolution (**c**-right) by OD = 64 mm, f_0 = 4.5 MHz. **d**, **e** Correlation and NMSE with respect to OD and f_0 for the theoretical mandala image (**c**-center). **f** The image plane location, Z_{target}, and its effect on Correlation and NMSE.

Moreover, the z coordinate of the image plane also plays a role in the image quality and the accuracy of the printed parts. For the example of the maple leaf pattern, Fig. 6f shows the Correlation and NMSE values for different z-levels of the image plane, z_{target}, for a transducer with OD = 50 mm. The optima of Correlation and NMSE happens at a z_{target} range of 16–20 mm, therefore, the optimum location of the image plane should be considered when the hologram is designed to achieve the best image quality and accurate printed parts. Other evaluating parameter such as SNR and PSNR with respect to the z-level of the image plane is shown in Supplementary Fig. 5c.

The polymerization progress is quantified by tracking the Si–H bond intensity in infrared (IR) measurements[51,52] of before and after print specimens of PDMS (two components system) as well as normally cured PDMS in an oven. The IR measurements are shown in Supplementary Fig. 3a where printed walls with 10% and 20 % DC measured right after print (~10 s printing time for the wall with 10 mm height) show the same amount of Si–H intensity as the normal heat cured PDMS after 24 h in the oven. This shows that the polymerization in HDSP has the same progress as the molded polymer and cured in the oven. Mechanical tensile tests revealed the difference in mechanical properties[1]. Following the DSP, the printed parts revealed consistent elastic modulus compared with the normally cured resin, although the tensile strength is different. Specifically, parts with a porous structure exhibit reduced tensile strength compared to the transparent parts. This indicates that the cavitation does not affect the material's elastic modulus, it does influence tensile strength, particularly in the printed structures with porosity.

It is indeed crucial to ensure consistent acoustic properties throughout the material, such as speed of sound and attenuation. Inhomogeneities in the resin can lead to disturbances in the desired acoustic patterning, adversely affecting the print quality. We could also print composite polymers (polymer mixed micro/nano solid particles)[1], however, the mixture should be homogenous too to avoid uneven scattering from the added particles.

The presence of air bubbles inside the resin should always be prevented prior to the printing, as bubbles can significantly disrupt the propagation of sound waves due to the marked difference in sound speed between air and resin. To mitigate this, we typically degas the resin in a vacuum chamber to remove large air bubbles and achieve a homogeneous material composition. Additionally, careful handling of the resin after degassing is essential to avoid reintroducing air bubbles into the resin. However, it's important to note that a small percentage of microbubbles may still remain dissolved in the resin after the degassing process. These microbubbles are generally smaller than the wavelength of the sound waves used and do not significantly interfere with wave transmission. Instead, they can play a beneficial role in the cavitation process as the weak points in the medium to initiate bubble generation, contributing positively to the overall printing mechanism.

DC plays an important role in the final microstructure of the printed parts. Higher DC results in more pores in the printed structure which can be related to the higher level of energy transmitted to the printing region and higher number of induced cavitation bubbles. Supplementary Fig. 3b-left shows a fully transparent part without any porosity printed with DC = 14% while Supplementary Fig. 3b-right shows that when DC is increased to 50% the porous structures with >100 µm width appear in the printed wall. Porous region width for different acoustic power and DC are systematically measured and plotted in Supplementary Fig. 3c. Decreasing DC and power leads to smaller porous regions. In this parametric study, we observed that from 100% DC down to 50%, the porous width was almost similar.

However, upon further decreasing the DC in steps of 10% down to 10%, we meticulously identified the specific DC level at which bubble clouds ceased to form. Through detailed inspection with smaller steps of 1% DC, we determined the DC threshold where no bubbles were observed was ~14%.

In our experiments, DC < 15% resulted in fully transparent parts. It is feasible that printing with lower DC values, demands more printing time than printing with higher ones. The printing time for Supplementary Fig. 3b-left with lower DC was observed to be about 30 s while Supplementary Fig. 3b-right took about 15 s. Supplementary Fig. 3d investigates the pulse interval effect on porosity size for different DCs.

Discussion

We introduced a holography-based DSP in which instead of voxel-by-voxel printing in the previously introduced DSP process[1], the whole image of cross sections are projected to the target planes at once using acoustic holograms. The patterned ultrasound pressure at the image pixels induces cavitation bubbles where the printing material undergoes instant polymerization and solidification via sonochemical reactions. SCL and high-speed imaging experiments shed more light on the HDPS process and how the chemically active regions can be pattered using acoustic holograms. The effects of hologram design, frequency, transducer size and hologram manufacturing method in the accuracy of printed parts are discussed. Material and porosity characterizations are also provided.

Besides the accuracy of produced pressure patterns at the target planes, their uniformity also plays an important role in the accuracy of the printed parts. The pressure values of the image pixels could reach high values but if these values were not uniform, the printed pattern would not be uniform either and pixels with high values create a high level of polymerization and polymer deposition while low-pressure pixels possess less deposition. This issue creates waviness and thickness deviation on the printed patterns. The reason behind the existence of porous and transparent regions in our printed parts (e.g., Supplementary Fig. 3b-right) can be explained by this phenomenon as well. The transparent region is created by the low-pressure level pixels while the porous regions are created by high-pressure level pixels. To address these challenges, advancing our reconstruction algorithms to better manage the uniformity of the pressure patterns is essential. Implementing sophisticated computational techniques that can dynamically adjust and optimize pressure distributions will be a crucial focus of our future research efforts. This approach will enhance the overall quality and consistency of the printed objects, reducing anomalies and uniformity in the final products.

Furthermore, in the pursuit of advancing HDSP technology, the integration of active/dynamic acoustic holograms presents a substantial opportunity for enhancement. Programmable acoustic holograms, capable of actively generating desired acoustic fields for various geometries in real time, can be a substantial development[53–55]. Analogous to Digital Micromirror Devices used in optics, the Spatial Ultrasound Modulator (SUM) exemplifies this innovation[54,55]. Utilizing active acoustic holograms such as SUM significantly enhances HDSP's capability, enabling the creation of complex, fully three-dimensional printed objects with intricate details. However, the current form of HDSP utilizing passive hologram in this paper could have direct applications in printing the body as the complexity of the desired objects is limited.

The present work introduces a significant advancement in the dimensionality of sound-based printing techniques, transitioning from the point-based approach of DSP, to employing acoustic holography. This method allows for the manipulation of acoustic fields to simultaneously create an image of the entire layer. This paradigm shift is similar to the evolution observed in the photopolymerization printing processes which initially originated from the laser point-based SLA. SLA utilized a methodical approach, employing a laser to solidify resin selectively, tracing specific areas one at a time in a one-dimensional (1D) manner. Subsequently, the introduction of DLP represented a significant evolution in printing speed and efficiency, shifting from SLA's sequential, point-by-point curing method, to a more efficient, 2D strategy. By projecting entire cross-sectional images onto the printing platform, DLP facilitates the simultaneous curing of whole layers, significantly enhancing both speed and efficiency in the photopolymerization printing process.

Methods

Acoustic equipment

Three single-element flat transducers of various dimensions and frequencies were used in this study. These commercially available flat transducers (American Piezo Co., USA) have active elements of ~0.9–1.1 mm thicknesses, with OD = 50, 35 and 25 mm with center frequency, f_0, of 2.28, 1.86 and 2.24 MHz, respectively. Each transducer was encapsulated with aluminum housing, as provided by the manufacturer. The efficiency of the transducers in converting the electrical power to acoustic power was around 49%, as reported by the manufacturer. To drive the transducers the power generator device TPO-102 (Sonic Concept Inc., USA) with 4–210 Watt power range and 50 Ω output impedance was used with a built-in sin function generator. A step-down electrical matching unit (model #90-4496, American Piezo Co., USA) to connect the transducers with 20 Ω impedance to the power generator with 50 Ω was employed to ensure the best electrical matching between the transducer and the power generator. To minimize the distortion of the passing wavefront and reflection as well as maintaining the acoustic power transmission, a thin shell-type barrier separates the water medium from the built chamber. Moreover, to maintain a good energy transfer and balanced coupling between the transmission hologram and the transducer, we used mechanical clamping (bolting) accompanied by the epoxy paste matching layer, ensuring the best combination for acoustic matching. The conductive thermal paste is homogeneously distributed to the surface of the phase plate by spin coating (WS-400B/Lite) at ~3500 RPM. In order to acquire the pressure patterns a needle hydrophone with 0.2 mm diameter (model no. D1602) along with the hydrophone booster amplifier (Precision Acoustics Ltd., UK) is used.

The speed of sound in deionized (DI) water at the laboratory temperature as ~1480 m/s and the transmission phase plate material as ~2430 m/s was measured using through transmission technique[56,57] with needle hydrophone while the speed of sound in PDMS with different mixing ratios was obtained via high-speed images to be used for the further finite element simulations. Mostly we used 10:1 mixing ratio of the base PDMS to the curing agent, and the speed of sound obtained was ~1040 m/s. Furthermore, we performed the pressure mapping with an in-house setup including an acrylic test tank of 1 × 0.75 × 0.75 m dimension filled with DI water with a needle hydrophone mounted on a computer-controlled positioner. An oscilloscope (Tektronix DPO2400) was used to acquire the needle hydrophone signal which was then connected to MATLAB R2020b to store and post-process the signals. The positioner movement and the data acquisition from the needle hydrophone were synchronized with the computer and triggered by the input burst pulse to the transducer.

Printing material preparation

SYLGARD 184 kit (Krayden, Canada) is used as the printing material in this paper. The PDMS system (monomer and curing agent) was mixed with the defined mixing ratios. The mixture was degassed using a vacuum for 45 min. The PDMS system was colored by adding the 2% w/w oil-based dye (Winsor & Newton, UK) to the base monomer.

Holography-based SCL experiment and high-speed imaging

A 1 mM solution of luminol (3-aminophthalhydrazide, Sigma-Aldrich, Canada) is prepared, and the pH is adjusted to 12 using NaOH (Sigma-

Aldrich, Canada). The pH is continuously monitored in real time using a pH 315i meter (Wissenschaftlich-Technische Werkstätten, WTW, GmbH, Germany). Subsequently, 0.5 M sodium carbonate (Na_2CO_3) is added to the solution. The sodium carbonate is produced by heating sodium bicarbonate ($NaHCO_3$, commonly known as baking soda) to 100 °C.

Luminol solution is poured inside a build volume that is used for printing material container and placed in front of the flat transducer with a hologram attached with a distance of the designed object plane (20 mm). To reduce the ambient light for capturing SCL images while sonication, we performed the experiment inside a dark room. Single lens EOS 500D (Canon, Japan) camera is used for capturing images of sonochemical reactions. The exposure time of the DSLR camera was set to a maximum 30 s to ensure capturing the blue SCL light from desired geometries.

High-speed imaging performed with Fastcam SA-Z (Photron Inc, USA) high-speed camera. The high-speed imaging experiment presented in Fig. 3 was recorded with 6000 frames/s and a 6× magnification lens. To improve the brightness of the footages, Halogen light source is employed through all the experiment.

Volume deposition rate in HDSP vs. DSP

The polymerization rate within our HDSP system can be correlated with acoustic power and pressure, although with certain complexities inherent to the process. Importantly, in HDSP, the polymerization rate is influenced not only by the delivered acoustic power but also by the DC of the transmitted acoustic power applied to the resin.

To quantify this relationship in our system, we conducted a series of experiments in which we systematically varied both the acoustic power and the DC delivered to the resin. We have documented these variations and their impact on the printing time required to generate a solid wall by extruding a holographically generated line. This is detailed in Supplementary Fig. 3c, which illustrates the combination of power and DC with the printing time.

We have conducted a more detailed analysis and included additional data in Supplementary Fig. 4. This figure illustrates our parametric study on printing a wall with dimensions of $15 \times 1 \times 20\ mm^3$, as depicted schematically in Supplementary Fig. 4d.

We have expanded our analysis to include a new representation that specifically illustrates the relationship between printing power and printing time when the DC is varied, as shown in Supplementary Fig. 4a. We observed that increasing the DC results in extended printing times. Additionally, we introduce the concept of interaction strength, σ (W), calculated by multiplying the acoustic power (W) and the DC (%). Supplementary Fig. 4b demonstrates how this interaction influences the printing time, allowing us to derive corresponding polymerization rates under these conditions.

This analysis enables us to establish a quantifiable correlation between acoustic power, DC, and the polymerization rate, in terms of a volumetric deposition rate (VDR) function, given in Eq. 1. Our findings indicate that the total power required to print geometries of varying circumferential lengths differs, even though the intensity needed for printing each voxel remains constant. Consequently, to enhance the versatility of the VDR function presentation, we incorporated the intensity used in the parametric study, calculated as power divided by the circumferential area of the voxels targeted by acoustic holography for solidification. Supplementary Fig. 4c shows the plot of this numerically derived VDR function, modeled using a second-order polynomial (with $R^2 = 0.9564$):

$$\begin{aligned} \mathrm{VDR}\,(I,\mathrm{DC}) &= a_0 + a_{10}I + a_{01}\mathrm{DC} + a_{20}I^2 \\ &\quad + a_{11}I.\mathrm{DC} + a_{02}\mathrm{DC}^2 \\ \text{where}: \Big\{ a_0 = 1.24\times10^4,\ a_{10} = -2.88\times10^4,\ a_{01} &= -725.89, \\ a_{20} = 1.96\times10^4,\ a_{11} = 982.74,\ a_{02} &= 11.53 \Big\} \end{aligned} \quad (1)$$

where $I = \frac{P}{A_{\mathrm{ROI}}}$ is the acoustic intensity on the image with area of A_{ROI} and delivered acoustic power P. The VDR function is based on two key input parameters, intensity of the printing, I (W/mm^2) and DC. The results are clearly depicted in Supplementary Fig. 4c, which shows nonlinear traits. The quadratic nature of the numerically obtained VDR function is consistent with the quadratic-like trends observed in Supplementary Fig. 4a, b.

The time saved by HDSP due to stationary source, and not moving the focal point as in DSP, translates directly into faster overall printing speeds. The ability to solidify a large area at once, rather than point-by-point, is a clear advantage in scenarios where production speed is a critical factor. We have experimentally compared the printing of a wall of $15 \times 1 \times 20\ mm^3$ obtained by the two methods. Since we know the total volume of the printed part, and by selecting a modest power/feed rate setting for both methods of DSP and HDSP, the time taken for complete printing can be measured. The printing time for HDSP using 30 W and DC 50% (electrical input) was ~30 s while for DSP with 240 mm/min feed rate, the printing took 12.56 min. Comparing the printing time for HDSP vs. DSP, we can conclude that since the HDSP has more voxels to simultaneously print, it requires much higher energy compared to the DSP, and that's why it is faster. The printing time of HDSP is calculated using VDR and the printing time for DSP is path length divided by the feed rate of the source. Therefore, printing time can be experimentally obtained for the HDSP vs. DSP. Supplementary Table 1 shows this comparison in detail.

3D scanning and accuracy measurement of holograms

We used Formlabs 2.0 and 3.0 to fabricate the holograms. High-temperature as well as Clear resin was used with acceptable speed of sound measured between ~2650 and ~2430 m/s, respectively. The advantage of incorporating high-temperature resin is that it can withstand the temperature increase caused by the high-intensity passing wave, without deforming and damaging the whole structure of the holograms.

To assess the accuracy of the fabricated thickness pattern on the transmission holograms, we used 3D measuring laser Confocal Microscopy (Olympus, Lext OLS4100, Japan) with measuring accuracy down to 80 μm. The point clouds were then imported to CATIA V5 followed by deviation analysis with the original theoretical hologram 3D model.

Hologram calculation and COMSOL 3D simulations

The retrieved phase pattern required for the acoustic holography using transmission phase hologram was calculated with the IAS method[35], performed in Matlab2020b. The phase pattern was then converted to the thickness map of each hologram which was then fabricated with Formlabs 2.0 SLA printer. Next section briefly describes a protocol for generating a required acoustic field and printing for HDSP. To validate the accuracy of the projected field by holograms, 3D finite element simulations were conducted in COMSOL Multiphysics 6.0, acoustic module through a high-performance computing center with 32core CPU and 500GB RAM.

HDSP process flow

The working flow of the HDSP to print an object (Supplementary Fig. 1) begins by retrieving the phases necessary for creating the complex holographic field. This is done by preparing binarized image(s) of the cross-section of the objects to be printed, denoted as R^j (j indicating the index of each image) placed at $z = z_t^j$. These images are used to build the complex pressure field as:

$$p_t^j(x,y,z) = R^j(x,y,z)e^{i\phi_t^j(x,y,z)} \quad (2)$$

where φ_t^j is initially set to a random value. Then angular spectrum method takes the complex pressure field in the spectral domain of

$\mathbf{k} = (k_x, k_y, k_z)$ which can be found by 2D Fourier transform as Eq. 3:

$$P_t^j(k_x, k_y, z_t^j) = \int\int_{\infty} p_t^j(x, y, z_t^j) e^{-j(k_x x + k_y y)} \mathrm{d}x\mathrm{d}y \tag{3}$$

and employs the propagator function H,

$$H(k_x, k_y, \pm z_t^j) = e^{ik_z(\pm z_t^j)} \tag{4}$$

to propagate it back to the hologram plane at $z = 0$:

$$P_h^j(k_x, k_y, 0) = P_t^j(k_x, k_y, z_t^j) H(k_x, k_y, -z_t^j) \tag{5}$$

where $k_z = \sqrt{k^2 - k_x^2 - k_y^2}$, with k being wavenumber in the medium. In Eq. 3, a positive sign corresponds to the forward propagation toward the target plane, while a negative sign corresponds to the backward propagation toward the hologram plane. Finally, the 2D inverse Fourier transforms the complex pressure from the spectral domain to the spatial domain as:

$$p_h^j(x, y, 0) = \frac{1}{4\pi^2} \int\int_{\infty} P_h^j(k_x, k_y, 0) \mathrm{d}k_x \mathrm{d}k_y \tag{6}$$

The phase map of the backpropagated complex field on the hologram plane (Eq. 6) can be retrieved as ϕ_h^j. Next, the retrieved ϕ_h^j and imposed constrains at the source amplitude are used to continue the iteration and reconstruct the target object cross-section image, A^j. The algorithm iteratively propagates the complex field back and forth between the object plane at $z = z_t^j$ and the source plane at $z = 0$, while imposing the source and desired target amplitude, so that the reconstructed pressure image A^j converges to the reference pressure imageR^j. In each iteration step, the reconstructed image quality check will ensure the minimum error with the true image of the object. The evaluating criteria for measuring the quality of the reconstructed image can be mean squared error (MSE), NMSE, SNR and Correlation (see section "Image quality analysis"). Finally, the total phase map $\Phi_h(x, y)$ on the hologram plane necessary for the complex holographic field can be obtained by summation of all the retrieved phase maps, ϕ_h^j. After obtaining the phase map, the required complex acoustic field can be fine-tuned in its two constituents, the required power and the obtained phases. The acoustic power required for igniting the solidification can be adjusted by the pressure amplification, PA, which can be obtained theoretically for each hologram as PA^j. To generate a complex geometry, the input power P_{in} must be adjusted in accordance with the experimentally determined threshold power required for generating a single voxel, $P_{\text{thrsh, voxel}}$. This input power can be found using Eq. 7, which was derived from experimental data.

$$P_{in} = P_{thrsh,\,\text{voxel}} \times \left(\frac{PA_{voxel}}{PA^j}\right) \tag{7}$$

Next, the phase map Φ_h can be converted to thickness map and fabricated using $h = \Phi_h/(k_m - k_h)$, where k_h and k_m correspond to wavenumber in hologram material and medium, respectively. In this step, to prevent the formation of sudden artifacts, we bound the Φ_h values to be within 0–2π. Finally, the complex acoustic field will be ready to ignite the printing within the region of interest. Supplementary Fig. 1 illustrates the process flow of the HDSP.

Material characterization

To evaluate the effecting parameters on the printing process of HDSP, further characterization along with input parametric analysis was performed. A line object created by HDSP and extruded 10 mm in z-direction to form a wall, was chosen for this experiment. From the parametric analysis of the printed walls, it was observed that the dominating input parameters affecting the printing process are, input power, DC% and feed rate. Supplementary Fig. 3c presents the relation between power, printing time, DC% and microstructure width form within the printed walls. First of all, increasing the power and DC% separately led to decreasing printing time, since more energy will be delivered to the printing ROI, while causing the denser bubble cloud formation in some locations within the printing object due to increased cavitation pressure. However, decreasing the DC% was proved to diminish the presence of cavitation bubble clouds and results in more transparent objects. As such comparison, the image on the right side of Supplementary Fig. 3b shows a part with bubble cloud pillars formed within the structure printed with 50% DC and a few seconds printing time, while the image on the top depicts a fully transparent wall with the same power and 14% DC but relatively longer printing time. The DC% is a relative term expressing the ratio of burst signal duration to the interval time between consecutive bursts. Supplementary Fig. 3d shows a box plot depicting the difference in measured width of the bubble cloud pillars formed under conditions of 2.5 and 5 ms intervals, both with an average power of 6 W. The regression line represents the trend observed in the data. Hence, altering the interval of the input signal could be another affecting parameter to control the cavitation bubble cloud formation inside the printing part.

Image quality analysis

In order to have a precise comparison of the generated images of the printing object and the original image, a frequency range of 1.5–4.5 MHz with OD of transducer between 25–100 mm was considered. First, the original binary image of the desired object to be printed with a width of 20 mm at the base point of evaluation with $f_0 = 1.5$ MHz and OD = 2 5 mm was selected with each pixel value one-fifth of the wavelength with 126 × 126 size of image. By conserving the object width for each case through padding and resizing the image matrix, a reconstructed image of the desired object can be achieved. Next, the obtained images were resized back to the 126 × 126 pixels using interpolation without reducing the content followed by normalization, where can be compared with the base point image.

The equation for the Correlation between the two images can be found by Eq. 8[58]:

$$\text{Correlation} = \frac{\sum_j \sum_i (R_{i,j} - \bar{R})(A_{i,j} - \bar{A})}{\left(\left(\sum_j \sum_i (R_{i,j} - \bar{R})^2\right)\left(\sum_j \sum_i (A_{i,j} - \bar{A})^2\right)\right)^{0.5}} \tag{8}$$

where R is the reference image and A is the reconstructed image. The bar represents the mean value of the image. The NMSE formula can be represented as Eq. 9[42]:

$$\text{NMSE} = \frac{||R - A||_2^2}{||R||_2^2} \tag{9}$$

Other than evaluating parameters discussed in Fig. 6d, e, PSNR and SSIM[59] assist to compare the generated image and actual image of the printing object, more accurately. Hence, according to the PSNR equation given in Eq. 10 as:

$$\begin{aligned} \text{PSNR} &= 20\log_{10}\frac{A_{\max}}{\sqrt{\text{MSE}}}, \\ \text{MSE} &= \frac{1}{m}\sum\sum(A_{i,j} - R_{i,j})^2 \end{aligned} \tag{10}$$

Supplementary Fig. 5a, b illustrates the PSNR and normalized SSIM, demonstrating the direct relation of the frequency, f_0 and source aperture, OD, on image quality for the 20 mm image to be generated at

20 mm distance target plane. By increasing the frequency and transducer OD, the PSNR of the obtained images of the object improves and structural similarity between the desired image and reconstructed image increases. Moreover, by keeping the source aperture and frequency constant, the distance of the desired object plane from the source can highly affect the resolution of the object. Supplementary Fig. 5c blue shows the dependency of the object plane location to the SNR for the 50 mm transducer with 2.28 MHz frequency. As can be seen for z_{target} range between 16 and 20 mm, we can expect better SNR. Also, the PSNR of the reconstructed image vs. target plane position can be seen in Supplementary Fig. 5c red for the 50 mm transducer and 2.28 MHz frequency. The better SNR and PSNR can be achieved with a 16–20 mm distance of the object plane from the source. Hence, improved peak amplitude and less noise and side lobes can be achieved by wise selection of the effective parameters.

Robot's trajectory in HDSP

The robot's end effector, where the printing platform is attached to, trajectory and velocity need to be calculated based on the nature of the printing mechanism in HDSP using a robotic arm (Supplementary Fig. 7a). The printing location in HDSP, which is the image plane, is stationary while the printing platform (end effector) moves in the working space carrying already printed object. Therefore, in order to preserve constant printing speed and printing direction at the image plane, an inverse kinematic approach is developed for HDSP to generate the trajectory and velocity of the platform for a given part geometry.

Assuming the part geometry follows a curve $\mathbf{C}^0(u)$, a virtual curve as shown in Supplementary Fig. 7b, where u is the curve parameter. This curve is defined in the printing coordinate system's (PCS) origin and discretized by length Δs into N elements. $\mathbf{C}^k(u)$ represents a family of curves where kth element of this curve passes through the PCS's origin and $k = 0, \ldots, N$. In order to keep the printing direction constant (along the *z-axis* of PCS), the tangent of $\mathbf{C}^k(u)$ at $z = 0$, $\mathbf{V}_0^k$ should be coincident with the z-axis. $\mathbf{V}_0^k$ can be calculated as

$$\mathbf{V}_0^k = \left.\frac{d\mathbf{C}^k(u)/du}{|d\mathbf{C}^k(u)/du|}\right|_{z=0} \cdot \Delta s \tag{11}$$

However, $\mathbf{V}_0^k$ creates an angle θ^k with z-axis as shown in Supplementary Fig. 7b, c. In order to compensate for θ^k and adjust the orientation of $\mathbf{C}^k(u)$ at PCS origin, $\mathbf{C}^k(u)$ is transformed by the following transformation

$$\mathbf{C}^k(u) = \begin{bmatrix} 1 & 0 & 0 \\ 0 & \cos(-\theta^k) & -\sin(-\theta^k) \\ 0 & \sin(-\theta^k) & \cos(-\theta^k) \end{bmatrix} \cdot \mathbf{C}^k(u) + \mathbf{V}_0^k \tag{12}$$

The trajectory of the end effector, $\mathbf{P}^k$, can be found using Eq. 13 for each kth element as

$$\mathbf{P}^k = \mathbf{C}^k(u)\Big|_{u=0}, \tag{13}$$

and the vector defining the orientation of the end effector, $\mathbf{n}_p^k$, can be written as

$$\mathbf{n}_p^k = \left.\frac{d\mathbf{C}^k(u)/du}{|d\mathbf{C}^k(u)/du|}\right|_{u=0}. \tag{14}$$

In order to maintain a constant printing speed, V_{pr}, at the location of the image plane, the end effector transitional velocity, V_e^k, can be calculated as

$$V_{\mathrm{e}}^k = \left|\mathbf{P}^k - \mathbf{P}^{k-1}\right| / \left(\left|\mathbf{V}_0^k\right| / V_{\mathrm{pr}}\right). \tag{15}$$

Therefore, for any given $\mathbf{C}^0(u)$, the trajectory, orientation and the transitional velocity of the end effector can be calculated using Eqs. 13–15, respectively. Supplementary Fig. 7b–f shows an example of a calculated trajectory at multiple steps during the printing of the object.

Data availability

The authors declare that the data supporting the findings of this study are available within the paper and its Supplementary Information files. Additional data are available from the corresponding author upon request.

Code availability

The open-source MATLAB, COMSOL Multiphysics codes and NC-code (generating path for robotic arm) used in this study will be available upon request.

References

1. Habibi, M., Foroughi, S., Karamzadeh, V. & Packirisamy, M. Direct sound printing. *Nat. Commun.* **13**, 1800 (2022).
2. Melchels, F. P. W., Feijen, J. & Grijpma, D. W. A review on stereolithography and its applications in biomedical engineering. *Biomaterials* **31**, 6121–6130 (2010).
3. Gissibl, T., Thiele, S., Herkommer, A. & Giessen, H. Two-photon direct laser writing of ultracompact multi-lens objectives. *Nat. Photonics* **10**, 554–560 (2016).
4. Kim, Y. T., Ahmadianyazdi, A. & Folch, A. A 'print–pause–print' protocol for 3D printing microfluidics using multimaterial stereolithography. *Nat. Protoc.* **18**, 1243–1259 (2023).
5. Rahim, T. N. A. T., Abdullah, A. M., & Md Akil, H. Recent developments in fused deposition modeling-based 3D printing of polymers and their composites. *Polym. Rev.* **59**, 589–624 (2019).
6. Olubummo, A. et al. Photothermal bleaching of nickel dithiolene for bright multi-colored 3D printed parts. *Nat. Commun.* **14**, 586 (2023).
7. Yang, Y., Ragnvaldsen, O., Bai, Y., Yi, M. & Xu, B. X. 3D non-isothermal phase-field simulation of microstructure evolution during selective laser sintering. *NPJ Comput. Mater.* **5**, 81 (2019).
8. Suslick, K. S., Eddingsaas, N. C., Flannigan, D. J., Hopkins, S. D. & Xu, H. The chemical history of a bubble. *Acc. Chem. Res.* **51**, 2169–2178 (2018).
9. Pokhrel, N., Vabbina, P. K. & Pala, N. Sonochemistry: science and engineering. *Ultrason. Sonochem.* **29**, 104–128 (2016).
10. Yusof, N. S. M., Anandan, S., Sivashanmugam, P., Flores, E. M. M. & Ashokkumar, M. A correlation between cavitation bubble temperature, sonoluminescence and interfacial chemistry – A minireview. *Ultrason. Sonochem.* **85**, 105988 (2022).
11. Koukouvinis, P., Bruecker, C. & Gavaises, M. Unveiling the physical mechanism behind pistol shrimp cavitation. *Sci. Rep.* **7**, 13994 (2017).
12. Abrahao, A. et al. First-in-human trial of blood–brain barrier opening in amyotrophic lateral sclerosis using MR-guided focused ultrasound. *Nat. Commun.* **10**, 4373 (2019).
13. Šarc, A., Kosel, J., Stopar, D., Oder, M. & Dular, M. Removal of bacteria *Legionella pneumophila*, *Escherichia coli*, and *Bacillus subtilis* by (super)cavitation. *Ultrason. Sonochem.* **42**, 228–236 (2018).
14. Soyama, H. & Korsunsky, A. M. A critical comparative review of cavitation peening and other surface peening methods. *J. Mater. Process. Technol.* **305**, 117586 (2022).
15. Packirisamy, M. & Habibi, M. Methods and systems for additive manufacturing. US patent 20200001533A1 (2020).
16. Habibi, M., Packirisamy, M. & Foroughi, S. Ultra active micro-reactor based additive manufacturing. US patent 20230339181A (2022).
17. Habibi, M., Packirisamy, M. & Forughi, S. Remote distance printing and its applications. PCTCA2024050618 (2024).

18. Kuang, X. et al. Self-enhancing sono-inks enable deep-penetration acoustic volumetric printing. *Science* **382**, 1148–1155 (2023).
19. Debbi, L. et al. Ultrasound mediated polymerization for cell delivery, drug delivery, and 3D printing. *Small Methods*. **2301197**, 1–11 (2024).
20. Yao, G. et al. Sound continuous production of thermosets. *Adv. Funct. Mater*. **2312736**, 1–11 (2023).
21. Weber, M., Hyvönen, J., Salmi, A. & Hæggström, E. Desktop direct sound 3D printing. In *IEEE International Ultrasonics Symposium* (*IUS*) https://doi.org/10.1109/IUS51837.2023.10307970 (IEEE, 2023).
22. Larson, N. M. et al. Rotational multimaterial printing of filaments with subvoxel control. *Nature* **613**, 682–688 (2023).
23. Skylar-Scott, M. A., Mueller, J., Visser, C. W. & Lewis, J. A. Voxelated soft matter via multimaterial multinozzle 3D printing. *Nature* **575**, 330–335 (2019).
24. Kuang, X. et al. Grayscale digital light processing 3D printing for highly functionally graded materials. *Sci. Adv*. **5**, eaav5790 (2019).
25. Truby, R. L. & Lewis, J. A. Printing soft matter in three dimensions. *Nature* **540**, 371–378 (2016).
26. Shusteff, M. et al. One-step volumetric additive manufacturing of complex polymer structures. *Sci. Adv*. **3**, 5496 (2017).
27. Regehly, M. et al. Xolography for linear volumetric 3D printing. *Nature* **588**, 620–624 (2020).
28. Kelly, B. E. et al. Volumetric additive manufacturing via tomographic reconstruction. *Science* **363**, 1075–1079 (2019).
29. Loterie, D., Delrot, P. & Moser, C. High-resolution tomographic volumetric additive manufacturing. *Nat. Commun*. **11**, 852 (2020).
30. Wang, B. et al. Stiffness control in dual color tomographic volumetric 3D printing. *Nat. Commun*. **13**, 367 (2022).
31. Madrid-Wolff, J., Boniface, A., Loterie, D., Delrot, P. & Moser, C. Controlling light in scattering materials for volumetric additive manufacturing. *Adv. Sci*. **9**, 2105144 (2022).
32. Marzo, A. & Drinkwater, B. W. Holographic acoustic tweezers. *Proc. Natl Acad. Sci. USA* **116**, 84–89 (2019).
33. Marzo, A. et al. Holographic acoustic elements for manipulation of levitated objects. *Nat. Commun*. **6**, 8661 (2015).
34. Memoli, G. et al. Metamaterial bricks and quantization of metasurfaces. *Nat. Commun*. **8**, 14608 (2017).
35. Melde, K., Mark, A. G., Qiu, T. & Fischer, P. Holograms for acoustics. *Nature* **537**, 518–522 (2016).
36. Chen, J., Xiao, J., Lisevych, D., Shakouri, A. & Fan, Z. Deep-subwavelength control of acoustic waves in an ultra-compact metasurface lens. *Nat. Commun*. **9**, 4920 (2018).
37. Prat-Camps, J., Christopoulos, G., Hardwick, J. & Subramanian, S. A manually reconfigurable reflective spatial sound modulator for ultrasonic waves in air. *Adv. Mater. Technol*. **5** https://doi.org/10.1002/admt.202000041 (2020).
38. Assouar, B. et al. Acoustic metasurfaces. *Nat. Rev. Mater*. **3**, 460–472 (2018).
39. Xie, Y. et al. Acoustic holographic rendering with two-dimensional metamaterial-based passive phased array. *Sci. Rep*. **6**, 1–6 (2016).
40. Gu, Y. et al. Acoustofluidic holography for micro- to nanoscale particle manipulation. *ACS Nano* **14**, 14635–14645 (2020).
41. Ma, Z. et al. Acoustic holographic cell patterning in a biocompatible hydrogel. *Adv. Mater*. **32**, 1904181 (2020).
42. Kruizinga, P. et al. Compressive 3D ultrasound imaging using a single sensor. *Sci. Adv*. **3**, e1701423 (2017).
43. Andrés, D., Vappou, J., Jiménez, N. & Camarena, F. Thermal holographic patterns for ultrasound hyperthermia. *Appl. Phys. Lett*. **120** https://doi.org/10.1063/5.0081565 (2022).
44. Jiménez-Gambín, S., Jiménez, N. & Camarena, F. Transcranial focusing of ultrasonic vortices by acoustic holograms. *Phys. Rev. Appl*. **14**, 054070 (2020).
45. Andrés, D., Jiménez, N., Benlloch, J. M. & Camarena, F. Numerical study of acoustic holograms for deep-brain targeting through the temporal bone window. *Ultrasound Med. Biol*. **48**, 872–886 (2022).
46. Melde, K. et al. Acoustic fabrication via the assembly and fusion of particles. *Adv. Mater*. **30**, 1–5 (2018).
47. Melde, K. et al. Compact holographic sound fields enable rapid one-step assembly of matter in 3D. *Sci. Adv*. https://doi.org/10.1126/sciadv.adf6182 (2023).
48. McMurray, H. N. & Wilson, B. P. Mechanistic and spatial study of ultrasonically induced luminol chemiluminescence. *J. Phys. Chem. A* **103**, 3955–3962 (1999).
49. Fernandez Rivas, D. et al. Sonoluminescence and sonochemiluminescence from a microreactor. *Ultrason. Sonochem*. **19**, 1252–1259 (2012).
50. Wood, R. J., Lee, J. & Bussemaker, M. J. Disparities between sonoluminescence, sonochemiluminescence and dosimetry with frequency variation under flow. *Ultrason. Sonochem*. **58**, 104645 (2019).
51. Murphy, E. C. et al. Tailoring properties and processing of Sylgard 184: curing time, adhesion, and water affinity. *J. Appl. Polym. Sci*. **137**, 1–10 (2020).
52. Esteves, A. C. C. et al. Influence of cross-linker concentration on the cross-linking of PDMS and the network structures formed. *Polymer* **50**, 3955–3966 (2009).
53. Xu, M., Wang, J., Harley, W. S., Lee, P. & Collins, D. J. Programmable acoustic holography using medium-sound-speed modulation. *Adv. Sci*. **10**, 2301489 (2023).
54. Ma, Z. et al. Spatial ultrasound modulation by digitally controlling microbubble arrays. *Nat. Commun*. **11**, 4537 (2020).
55. Ma, Z., Joh, H., Fan, D. E. & Fischer, P. Dynamic ultrasound projector controlled by light. *Adv. Sci*. **9**, 2104401 (2022).
56. Bakaric, M. et al. Measurement of the ultrasound attenuation and dispersion in 3D-printed photopolymer materials from 1 to 3.5 MHz. *J. Acoust. Soc. Am*. **150**, 2798–2805 (2021).
57. Derayatifar, M., Habibi, M., Bhat, R. B. & Packirisamy, M. Influence of 3D printing parameters on acoustic properties of metamaterials. In *IEEE International Ultrasonics Symposium* (*IUS*) 1–3 (IEEE, 2022).
58. Zhu, Y. et al. Fine manipulation of sound via lossy metamaterials with independent and arbitrary reflection amplitude and phase. *Nat. Commun*. **9**, 1632 (2018).
59. Zhou, W., Alan, C. B., Hamid, R. S. & Eero, P. S. Image quality assessment: from error visibility to structural similarity. *IEEE Trans. Image Process*. **13**, 600–12 (2004).

Acknowledgements

M.D. acknowledges the support of FRQNT (Fonds de Recherche du Québec, Canada) for providing the doctoral scholarship. The authors acknowledge the financial support from NSERC Discovery of R.B. and M.P., Concordia Research Chair and PSO grants of M.P.

Author contributions

M.H. and M.P. conceived the idea. M.H. designed the experiments and modeling. M.D. conducted theoretical investigation, simulation, experiment and visualization. M.H. and M.P. supervised the work. M.D. and M.H. equally contributed to the manuscript. M.D. and M.H. wrote the manuscript. R.B. and M.P. edited the manuscript and all authors contributed to the writing of the manuscript.

Competing interests

The authors declare the following competing interests: M.H. and M.P. are inventors of patents (US20200001533A1, US20230339181A1 and PCTCA2024050618). These patents are related to the topic covered in this manuscript. M.D. and R.B. declare no competing interests.

Additional information

Supplementary information The online version contains supplementary material available at https://doi.org/10.1038/s41467-024-50923-8.

Correspondence and requests for materials should be addressed to Muthukumaran Packirisamy.

Peer review information *Nature Communications* thanks David Collins, Ahmad Rafsanjani and the other, anonymous, reviewer(s) for their contribution to the peer review of this work. A peer review file is available.